Tuning of e_g electron occupancy of MnCo₂O₄ spinel for oxygen evolution reaction by partial substitution of Co by Fe at octahedral sites

Krystian Lankauf*[†], Karolina Górnicka[‡], Patryk Błaszczak[‡], Jakub Karczewski[‡], Jacek Ryl[‡], Grzegorz

Cempura[§], Marcin Zając[#], Maciej Bik[Ŧ], Maciej Sitarz[Ŧ], Piotr Jasiński[†], Sebastian Molin[†]

[†]Advanced Materials Center, Faculty of Electronics, Telecommunications and Informatics, Gdańsk

University of Technology, ul. G. Narutowicza 11/12, 80-233 Gdańsk, Poland

[‡]Advanced Materials Center, Faculty of Applied Physics and Mathematics, Gdańsk University of

Technology, ul. G. Narutowicza 11/12, 80-233 Gdańsk, Poland

[§]Faculty of Metals Engineering and Industrial Computer Science, Centre of Electron Microscopy for

Materials Science, AGH University of Science and Technology, al. A. Mickiewicza 30, 30-059

Kraków, Poland

[#]National Synchrotron Radiation Centre Solaris, Jagiellonian University, 30-392 Kraków,

ul. Czerwone Maki 98 Poland

[Ŧ]AGH University of Science and Technology, Faculty of Materials Science and Ceramics, al.

Mickiewicza 30, 30-059 Kraków, Poland

*e-mail: krystian.lankauf@pg.edu.pl

ABSTRACT:

To study the effect of partial Co substitution by Fe in the B-site of MnCo₂O₄ spinel on its physicochemical and electrochemical properties, a series of MnCo₂₋ₓFeₓO₄ powders (x=0.125; 0.250; 0.500; 0.750; 1.000) were synthesized by means of the sol-gel method. The produced powders were

characterized by powder X-ray diffraction (pXRD), scanning and transmission electron microscopy (SEM & TEM) coupled with energy dispersive spectroscopy (EDS), X-ray photoelectron and absorption spectroscopy (XPS & XAS), Fourier transformed infrared spectroscopy (FTIR), and inductively coupled plasma optical emission spectroscopy (ICP-OES). The electrocatalytic activity towards oxygen evolution reaction (OER) was evaluated in an alkaline environment (0.1 M KOH). From our findings, the activity increased with the addition of Fe up to x = 0.5, characterized by a decrease of overpotential at 10 mA cm$^{-2}_{GEO}$ from 406 mV for $MnCo_2O_4$ to 376 mV for $MnCo_{1.5}Fe_{0.5}O_4$, with a corresponding 44 mV dec^{-1} Tafel slope. It was identified that the OER-specific activity exhibits a volcano-type shape as a function of the e$_g$ occupancy at octahedral sites tuned by Co substitution with Fe.

Keywords: spinel; oxygen evolution; electrocatalysts; water splitting; element substitution

1. INTRODUCTION

The development of highly efficient energy storage and conversion technologies is crucial to meet the growing energy needs and to reduce the human impact on the environment. Hydrogen is prominent as a clean and abundant sustainable energy carrier and fuel [1–3]. Electrochemical water splitting is a promising process due to the abundance of the reaction substrate and safety of the byproduct, i.e. water and molecular oxygen, respectively. The efficiency of electrocatalytic water splitting is limited by its high energy consumption related to the overpotentials needed to sustain the electrolysis half-reactions: the cathodic hydrogen evolution reaction (HER) and the anodic oxygen evolution reaction (OER). Among these two processes, the OER is more challenging due to the sluggish kinetics and is thermodynamically less favorable, which is associated with the four-electron/proton-coupled transfer reaction pathway [4,5]. Therefore, the development of low-cost, highly active OER catalysts is an important task to reduce the reaction overpotentials, and hence the energy consumption of water splitting systems[6,7].

Transition metal oxides with the formula AB_2O_4 (where A and B are transition metal ions), named spinels after the representative $MgAl_2O_4$, have found interest in energy conversion systems due to their exceptional electrocatalytic properties [8,9]. Spinel oxides are composed of A-O tetrahedrons and B-O octahedrons, where A and B can contain the same or a different metal element. The valence equilibrium is maintained if cation A is in the +2 or +4 oxidation state and cation B is in the +3 or +2 oxidation state. Knowing the crystal field stabilization energy (CFSE) and ionic radii of the elements, one can "design" the spinel structure, predicting the positions of its constituent elements, and hence the valence state and electronic structure [10,11]. Various compositions, morphologies, structures, and valence states can be obtained through the deliberate choice of the preparation method. In brief, spinel oxides can be prepared by solid-phase [12,13], solution-phase [14,15] and vapor-phase methods [16–18].

One of the spinels with flexible applications is the manganese cobaltite spinel: $MnCo_2O_4$, which can be fine-tuned by chemical modifications [9]. Commonly, $MnCo_2O_4$ is described as an inverse spinel with the Mn cations preferring to occupy the octahedral site. Depending on the preparation method and thermal history, its physicochemical properties can be modulated by induced cationic distribution

changes. Wei et al. synthesized $MnCo_2O_4$ at 150, 300, 400, 500, 700, and 900 °C and observed that the average Mn valence state ranges from +3.2 to +3.7 depending on the synthesis temperature [19]. The OER studies exhibited a volcano shape of activity as a function of the Mn valence state with the peak of the trend around +3. Wang et al. employed the spray-pyrolysis route to prepare a mesoporous $MnCo_2O_4$ bifunctional oxygen electrocatalyst [20]. Both Mn_2O_3-like performance for oxygen reduction reaction (ORR) and Co_3O_4-like activity for OER were observed. The notable bifunctional activity resulted from the preferred Mn^{IV}- and Co^{II}-rich surface attained by the surface state engineering approach. A series of Fe-substituted $ZnFe_xCo_{2-x}O_4$ was prepared by Zhou et al. [21]. Fe substitution at 10-30 at.% facilitates the injection/extraction of electrons from oxygen. As a result, enlarged Co 3d and O 2p covalency occurred, associated with enhanced OER activity.

The ternary Mn-Co-Fe spinel oxides have already exhibited the promising properties for application in sustainable energy field. Liu et al. have synthesized the series of $MnCo_{2-x}Fe_xO_4$ (x = 0-0.7) spinel oxides by solid-state reaction for SOFC interconnect coatings. The Fe doping stabilized the cubic spinel structure and decreased the electrical conductivity obeying the small polaron hopping mechanism at 800 °C in air [22]. Elkholy et al. reported the ternary $MnCoFeO_4$ nanoparticles for high-performance supercapacitor application, exhibiting high energy and power densities with excellent long-term stability [23]. Kim et al. presented that the redox potential of $mnCoFeO_4$ differs than of mixture of component spinels (Co_3O_4, Fe_3O_4, Mn_3O_4) [24]. Furthermore, they demonstrated an economically viable approach for fabrication of high-performance MFC based anodes for lithium rechargeable batteries. However, to our knowledge, there is a lack of complex studies of ternary Mn-Co-Fe spinel oxides, with emphasis on optimal Co : Fe ratio, for OER electrocatalysis application.

Herein, we studied the effect of partial Co substitution by Fe in the B-site of $MnCo_2O_4$ on the physicochemical and electrochemical properties. A series of $MnCo_{2-x}Fe_xO_4$ powders (x=0.125; 0.250; 0.500; 0.750; 1.000) were synthesized by a facile sol-gel method. All materials were examined for their structural properties and OER electrocatalytic activity in an alkaline electrolyte (0.1 M KOH).

2. EXPERIMENTAL SECTION

2.1 Materials synthesis. Iron-substituted manganese cobaltite spinel oxides were prepared by a sol-gel EDTA-Citric Acid method similarly to in previous work [25]. Analytical grade $Mn(NO_3)_2 \cdot 4H_2O$, $Co(NO_3)_2 \cdot 6H_2O$, and $Fe(NO_3)_3 \cdot 9H_2O$ were dissolved in a minimum amount of deionized water in the right proportions to obtain stoichiometric products. In parallel, citric acid (CA) and ethylenediaminetetraacetic acid (EDTA) were dissolved in deionized water with the addition of an ammonia solution to allow EDTA dissolution. The specific molar ratio of the reagents was maintained, i.e. TMI:CA:EDTA = 1:2:1 (TMI –Total Metal Ions). The prepared solutions were mixed together and stirred on a magnetic stirrer at room temperature for 10 min and ammonia solution was added to maintain a pH level of 6. The precursor solution was heated to 90 °C and maintained under magnetic stirring for ~5 h until a dark gel was formed. The gel was transferred to a laboratory drier and dried at 90 ° for 2 h, at 120 °C for 5 h, and at 180 °C for 5 h. The obtained dry powder was ground in an agate mortar, placed in an alumina crucible and calcined in a muffle furnace in air at 400 °C for 1 h, again ground in the agate mortar, and further heat-treated in air at 800 °C for 2 h. The calcined powders were ball-milled in ethanol for 144 h (Zoz Gmbh, Rollermill RM1) in 20 mm diameter glass vials using yttria-stabilized zirconia (YSZ) spherical grinding media (φ1 mm) with a rotation speed of 100 rpm for agglomerate defragmentation to improve the electrocatalytic performance.

2.2 Characterization. Powder X-ray diffraction (pXRD) was conducted at room temperature on a Bruker D2 Phaser diffractometer with CuKα radiation (λ=1.5404 Å) and a Lynxeye XE-T detector in the range from 5 to 110 ° with 0.01 ° step size. Unit cell parameter calculation was performed by Le Bail refinement using the Fullprof software package [26]. Weight fractions of additional phases were estimated by Rietveld refinement performed using GSAS-II [27]. The *.cif files were downloaded from the Inorganic Crystal Structure Database and Crystallography Open Database [28,29].

The morphologies of the prepared powders were investigated using an FEI Quanta 250 FEG Scanning Electron Microscope (10 kV accelerating voltage, Everhart–Thornley detector) and a Cs-corrected Titan Cubed G2 60 300 (FEI) Scanning Transmission Electron Microscope (S/TEM). The chemical composition was examined using the ChemiSTEM EDX system based on four windowless Silicon Drift

Detectors (Super X). The powders for TEM investigations were prepared by placing a drop of water suspension containing the powder onto a copper grid followed by vacuum drying.

The specific surface area of the powders was measured using the N_2 adsorption technique (Quantachrome, NovaTouch LX1) according to the BET isotherm model. The samples were degassed prior to sorption measurement at 300 °C for 3 h under vacuum.

X-ray photoelectron spectroscopy (XPS) measurements were performed using an Axis Supra spectrometer (Kratos Analytical) to investigate the valence states of the Mn and Co in the $MnCo_2O_4$ spinel. The spectroscope was equipped with an Al Kα source. The pass energy and the spot size diameter were 20 eV and 2×0.7 mm, respectively. Metallic gold and copper were used for the instrument calibration. The CasaXPS 2.3.18 software on a Shirley background was used to analyze the obtained spectra. The XPS binding energies were corrected using the C 1s peak at 284.6 eV.

X-ray absorption spectroscopy (XAS) measurements of the $MnCo_{2-x}Fe_xO4$ samples were performed at the 04BM PIRX (former PEEM/XAS) beamline of the SOLARIS National Synchrotron Radiation Centre for the $L_{2,3}$-edge spectra of Mn, Co, and Fe. The PIRX beamline uses a bending magnet (1.31 T) to provide a photon energy range from 100 to 2000 eV with an energy resolution no lower than $2.5 \cdot 10^{-4}$ [30]. The beam spot size at the sample was 250 μm x 40 μm (horizontal x vertical). Powder samples were applied to carbon tape and located on the Omicron-type plate sample holder. XANES spectra were recorded using total electron yield detection mode (TEY) which reflects an information depth of several nm. Measurements were performed in UHV and at ambient temperature. The obtained data were processed in the Bessy software. The data were first normalized to the measured incident photon flux I_0. Further data processing steps consisted of subtracting a straight line fitted to the L_3 pre-edge region, dividing by a polynomial function fitted to the L_2 post-edge region, and normalizing to a maximum intensity of 1.

Fourier Transformed Infrared Spectroscopy studies in the Middle (MIR) and Far Infrared Range (FIR) were performed on a Bruker Vertex 70v spectrometer under vacuum conditions using the transmission technique. For sample preparation, ca. 2 mg of thoroughly ground powder was mixed with a reference

material (400 mg of KBr (Uvasol®, Merck) in MIR and 180 mg of polyethylene (Uvasol®, Merck) in FIR range) and pressed with a hydraulic press. To record the spectra, 256 scans and a resolution of 2 cm^{-1} were applied in the 4000–400 cm^{-1} (MIR) and 400–100 cm^{-1} (FIR) spectral ranges. The spectra were subsequently post-processed using the OPUS 7.2. software. First, the MIR spectra were cut within the 1000–400 cm^{-1} range, as no important bands occurred within the remaining part. Afterwards, three representative spectra (MCO, MCF500, MCF1000) were deconvoluted using the Handke method [31] and the Levenberg-Marquardt algorithm. During the deconvolution process, a set of Gaussian-Lorentzian bands was used which resulted in an RMS error of 0.05. Finally, the positions of all bands were estimated using the Peak Picking function, both before and after the deconvolution process.

2.3 Electrode preparation and electrochemical measurements. Glassy carbon rotating disk electrodes (RDE-GCE, 0.196 cm^2, ALS Co., Ltd) were used as support electrodes for the powder catalysts. Before the deposition of the catalyst inks, the RDE-GCE were polished for 5 min using 9, 3, and 1 μm polishing diamond solutions, sonicated for 10 min in deionized water and isopropanol, respectively, then dried overnight under ambient conditions. The catalyst and Super P Li Conductive Carbon Black (CCB) (Imerys Graphite & Carbon) powders were separately ball-milled in ethanol for 144 h using φ1 mm YSZ grinding balls. The spinel powder and CCB suspensions were mixed with K$^+$-exchanged Nafion solution in the appropriate proportion to obtain 1 mL of ink with a weight ratio of solids of 5:5:2 (Catalyst:CCB:Nafion). The K+-exchanged Nafion preparation has been described elsewhere [32]. Subsequently, the inks were sonicated in an ice-water bath for 30 min. Then 5 μL of ink was drop-cast onto the RDE-GCE rotating at 700 rpm, achieving a catalyst mass loading of 45.5 μg. All electrochemical measurements were performed in a custom-made three-electrode Teflon cell system in 0.1 M KOH aqueous solution (prepared from 1 M KOH Titripur from Merck, diluted with DI water ~12 MΩ). A coated RDE-GCE, a Pt coil, and a Hg/HgO in 0.1 M KOH solution (ALS Co., Ltd, Japan) were used as the working (WE), counter (CE), and reference (RE) electrodes, respectively. The electrochemical tests were performed on BP-300 (BioLogic) bipotentiostat connected in a rotating disk electrode (RDE) configuration (RRDE-3A Rotating Ring Disk Electrode Apparatus Ver.2.0, ALS Co., Ltd). Before each experiment, the electrolyte was purged with 99.995% O$_2$ for 30 min, then the gas flow

(50 mL min^{-1}) was maintained over the electrolyte to maintain the O_2/H_2O equilibrium. An electrolyte temperature of 25 °C was maintained by a Julabo F12 thermostat. All electrocatalytic experiments were performed using the same protocol. The disk electrode was conditioned by potential cycling 10 times in the range of 1.0–1.7 V vs RHE at a scan rate of 100 mV s^{-1}. Cycling voltammetry (CV) scans were performed in the non-faradaic potential region of 0.98 - 1.08 V vs RHE at scan rates of 10, 20, 40, 60, 80, 100 mV s^{-1} without RDE rotation for the double-layer capacitance (Cdl) estimation. The electrochemical active surface area (ECSA) was calculated assuming the reference capacitance value of 40 µF cm^{-2} for oxides [33]. The charge transfer resistance (R_{ct}) was calculated from the electrochemical impedance spectroscopy (EIS) measurements in the frequency range from 10 kHz to 0.1 Hz at 1.7 V vs RHE with an amplitude of 10 mV and a rotation speed of 1600 rpm. Fitting to the modified Randles equivalent circuit was performed with the EC-Lab® Software. CV scans for OER were performed in the range from 1.1 to 1.9 V vs RHE at a scan rate of 10 mV s^{-1} with a rotation speed of 1600 rpm. All measured potentials were converted to RHE by the experimental calibration of the Hg/HgO reference electrode against RHE (exemplary CV is shown in Figure S1) [34]. The reference electrode was calibrated under experimental conditions weekly to exclude non-negligible electrode potential differences [35]. The value of E_{Offset} against RHE equals the measured equilibrium potential of hydrogen electrocatalysis (HER/HOR) and was determined to be in the range of < -928; -920 > mV. For the OER polarization curves, the background correction was performed by averaging the positive and negative-going scans [34]. All potential values were iR-corrected to eliminate the solution resistance. The current density was normalized by the geometric surface area of the RDE-GCE (0.196 cm^2) (expressed in the unit mA cm$_{GEO}^{-2}$). The OER overpotential was calculated as the difference between the potential when the current density reached 10 mA cm$_{GEO}^{-2}$ and the standard potential of oxygen electrocatalysis (1.23 V). The specific activity was determined by current normalization using the BET-specific surface area of each oxide catalyst (expressed in the unit µA cm$_{OX}^{-2}$). For each material, at least 3 separate samples were prepared and tested.

The durability tests (chronopotentiometry at 10 mA cm^{-2}) were performed with commercial electrolyzer cell (ElectroCell, Micro Flow Cell) in 0.1 M KOH. The electrolyser cell consisted of Ti cathode, Zirfon®

Perl 500 UTP diaphragm (AGFA), and Sigracet 39 AA (SGL Carbon) carbon paper support as anode. The active geometrical area for both electrodes was 10 cm^{-2}. The anode potential was measured using leak-free LF-1 Ag/AgCl reference electrode (ElectroCell). Electrolyte circulation of 200 mL min^{-1} flow was forced using water pump (12V, 1.2 l min^{-1} , 1200 mA).

3. RESULTS AND DISCUSSION

3.1 Structure characterization. The powders, based on the general formula of $MnCo_{2-x}Fe_xO_4$, with x=0.125; 0.250; 0.500; 0.750; 1.000, are labelled as MCO, MCF125, MCF250, MCF500, MCF750, and MCF1000.

The chemical composition of the synthesized powders was analyzed by EDS and ICP-OES, and the results are presented in Table S1. Good agreement between the planned stoichiometry and the resulting powder composition was obtained. The main impurities, as detected by ICP were Na, Si, K, Ca, not exceeding 0.05 at. %.

The phase composition of the powders was studied using X-ray diffractometry. As shown in Figure 1b, the pXRD peaks of the ball-milled powders show the standard spinel $MnCo_2O_4$ cubic structure (space group Fd-3m, No. 227) [36]. The synthesized oxides were phase pure up to x=0.5 composition. A slightly visible additional peak (33°) indicating the existence of Mn and/or Fe oxide was observed for the MCF750 (Figure S2) and MCF1000 powders. Since the weight fraction of observed impurities calculated by Rietveld refinement was < 3% (Figure S3), the impurities are considered to be negligible in the terms of OER electrocatalysis.

In comparison to our previous work, the addition of ethylene glycol was omitted during the synthesis, which ensured crystallization of pure, single-phase material [25]. The calcination temperature was also increased from 600 °C to 800 °C. At the lower calcination temperature, Mn and Fe oxides were detected in the powders by pXRD (Figure S4).

Figure 1c shows the shift of the position of the characteristic peak (311) towards lower 2θ angles with the increasing Fe content, demonstrating the incorporation of iron into the structure and resulting in enlargement of the lattice size. For coordination number VI (the octahedral position), the ionic radius of

Fe^{3+} (high spin) is 0.645 Å, whereas the radius of Co^{3+} (high spin) is 0.61 Å. The ball-milling process reduces the particle size and influences the average crystallite size, as determined by the broadening of the peaks (according to the Scherrer equation).

The Le Bail refinement results presented in Figure 1d show that the lattice parameter scales almost linearly with the higher Fe substitution (data in Table S2). The dashed line presents Vegard's slope calculated based on unit cell data taken from the literature, i.e. MnCo$_2$O$_4$ (ICSD ID 291115) and MnFe$_2$O$_4$ (COD ID 2300585) [28,29].
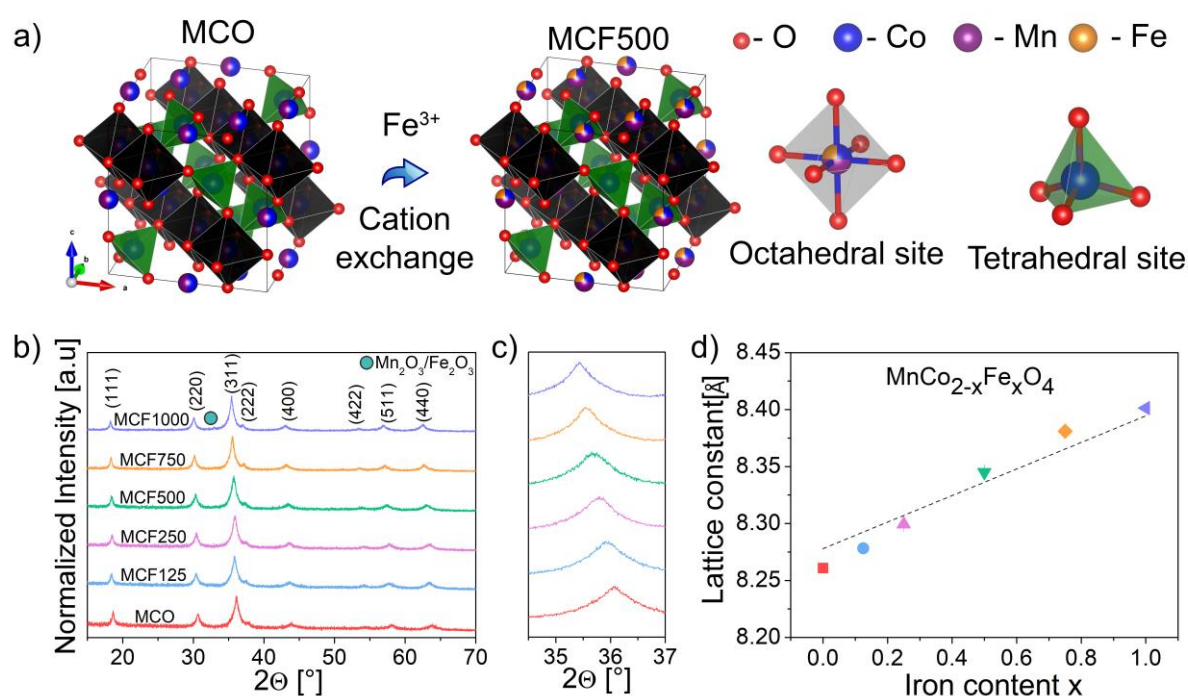
Figure 1. (a) Inverse cubic spinel structure (B[AB]O$_4$) with highlighted octahedrally and tetrahedrally coordinated transition metal cations. (b) pXRD patterns of ball-milled MnCo$_{2-x}$Fe$_x$O$_4$ powders, (c) zoom-in of the patterns showing the main reflection (311) shift, (d) and calculated lattice parameters.

Figure 2a shows the SEM image of the morphology of the ball-milled MCF500 powder. The sample is composed of irregularly shaped grains with diameters in the range of 50 to 200 nm. All other MnCo$_{2-x}$Fe$_x$O$_4$ powders have similar morphology and grain size distribution (Figure S5). The chemical compositions of the synthesized powders were evaluated by EDS/ICP analyses, which confirmed the desired stoichiometry (Table S1). The powders' specific surface area, measured with the N$_2$ adsorption

technique presented in Table S2 shows that for all Fe-substituted materials, the specific surface area was ~23 m^2 g^{-1}, which corresponds to a characteristic particle size of ~50 nm.

The transmission emission electron microscopy image (TEM) in Figure 2b further confirmed the grains' size and their irregular morphology, also demonstrating the plate-like structure of some grains, possibly resulting from the ball-milling process. As shown in Figure 2c, the HRTEM image displays the lattice fringes with an interplanar distance of 0.483 nm, which corresponds to the (111) plane of MnCo$_{1.5}$Fe$_{0.5}$O$_4$ and is consistent with the d-spacing of the (111) plane derived by Le Bail refinement (0.482 nm). Furthermore, the selected area electron diffraction (SAED) patterns (Figure S6) demonstrate the well-defined crystalline cubic structure of the Fd-3m space group. Dispersion of the constituent elements (Mn, Co, Fe) was observed by TEM-EDS elemental analysis (Figure 2e–g). However, segregation of Mn and Fe in some spots indicates the inherence of impurities in the form of Mn and Fe oxides in such a low amount that it was not observed earlier in the pXRD histograms.
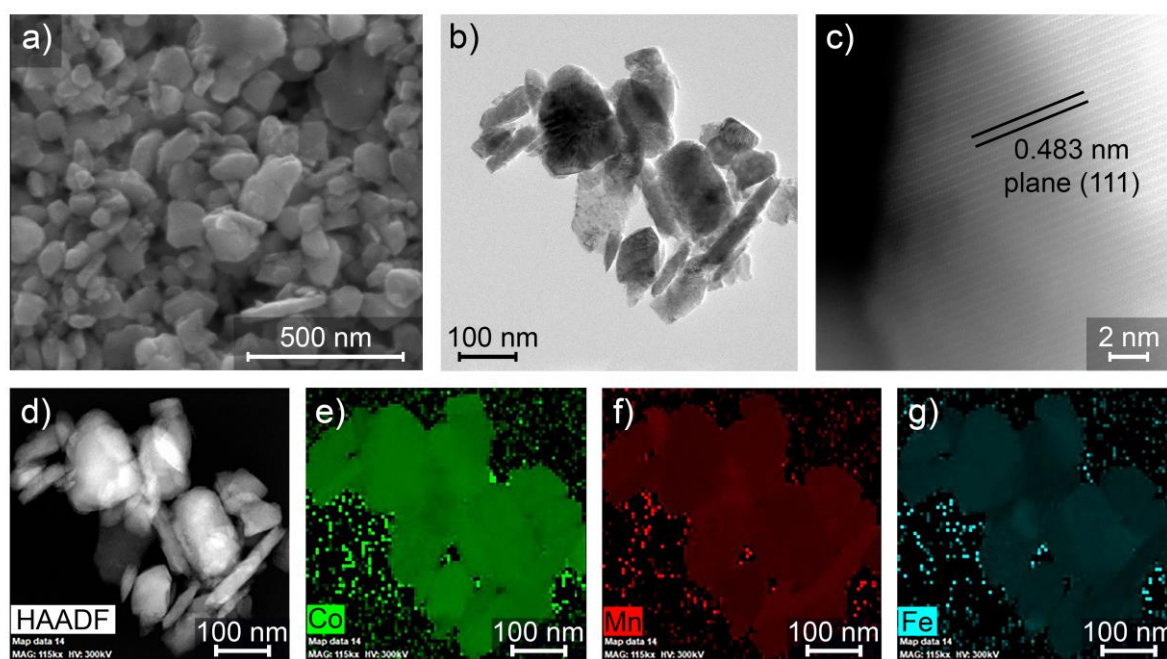
Figure 2. (a) SEM image (x100,000 magnification) of synthesized and ball-milled MCF500 powder, (b) BF-TEM image, (c) HRTEM image, (d) HAADF-STEM image, (e–g) and corresponding STEM-EDS elemental maps of (e) cobalt, (f) manganese, and (g) iron.

Figure 3 displays the XPS spectra of the MCFx (x=0.125; 0.250; 0.500) samples. The Mn2p spectra are presented in Figure 3a. Three oxidation states of manganese (II, III, IV), which are probable to co-exist in the inverse spinel structure, are characteristic because of the significant multiplet splitting observable in the XPS spectra, making a quantitative analysis challenging [37]. Due to the above, the collected spectra were fitted with respect to the most likely occurring Mn^{3+} species. Fitting parameters based on the Mn_2O_3 parameters provided by Biesinger et al. are presented in Table S3. For all samples, the main peak (Peak 2, ~641.9 eV) area is lower than that of the reference Mn_2O_3 ($< 44.5\%$), suggesting the observation of the influence of other Mn species on the collected spectra. In general, peaks at lower and higher binding energies have a higher area than the reference, indicating the existence of both Mn^{2+} and Mn^{4+}, respectively. For a detailed analysis of surface Mn valency, a more sophisticated method is necessary and is described in the next section. Co2p spectra are demonstrated in Figure 3b. It is clearly visible that Co is, as expected, present in two forms: Co^{2+} and Co^{3+}. For samples the MCF250 and MCF500, additional slightly visible peaks are observed at ~779 eV, indicating the formation of new Co-O species, which may be related to the element segregation observed by the TEM studies. A quantitative analysis was omitted due to the influence of Auger signals from the Fe [38,39]. The Fe2p spectra presented in Figure 3c are highly influenced by Co-LMM Auger peaks. However, a higher ratio of Fe^{3+} in the $MnCo_{2-x}Fe_xO_4$ with higher x is still observed.
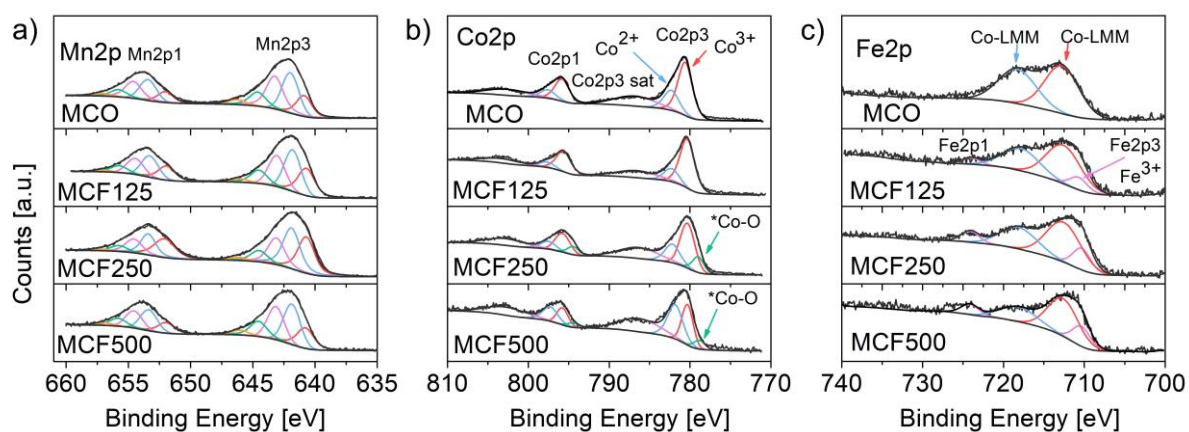

Figure 3. (a) Mn2p, (b) Co2p and (c) Fe2p X-ray photoelectron spectra of MCO, MCF125, MCF250, MCF500 powders.

X-ray absorption near-edge structure (XANES) spectra using total electron yield (TEY) were carried out to explore the impact of Fe substitution on the $MnCo_{2-x}Fe_xO_4$ spinels. L_3-edge XANES involves excitation of $2p_{3/2}$ electrons into unoccupied states of 3d character and was used to examine the valence of the Mn, Co and Fe. Additionally, reference samples, known for the stable and specified valence of their constituent transition metals cations, i.e. spinel oxides: Co^{2+} in $CoAl_2O_4$, Co^{3+} in $ZnCo_2O_4$, Co^{2+} and Co^{3+} in Co_3O_4, Fe^{3+} in $ZnFe_2O_4$, and oxides: Mn^{2+} in MnO, Mn^{3+} in Mn_2O_3, Mn^{4+} in MnO_2, were compared [40–43]. All observed Mn XANES spectra of the examined $MnCo_{2-x}Fe_xO_4$ spinels, as presented in Figure 4a, were close to that of the Mn_2O_3 reference with the main peak at ~642.2 eV corresponding to Mn^{3+} in octahedral coordination. Slight shoulders observed at ~640.3 eV indicate a small share of Mn^{2+} in most of the examined spinels. Moreover, the samples exhibited a pronounced, higher energy shoulder at ~643.1 eV corresponding to Mn^{4+}. Unlike the other stoichiometries, changes in the Mn valence for MCF1000 were observed. The amount of Mn^{4+} decreased in favor of Mn^{2+}, which is indicated by the less pronounced peak at the higher energy of ~643 eV and the more pronounced one at the lower energy of ~640 eV. For most of the samples, the observed mixed Mn valence complies well with the inverse spinel model proposed by Bordeneuve [44].

The Co L_3-edge XANES of the basic $MnCo_2O_4$ (Figure 4b) indicates a mixture of Co^{3+} and Co^{2+} with a high/low energy peak ratio of Co^{3+}/Co^{2+} close to 1, confirming the inverse spinel structure. It is important to highlight the fact that with higher Fe substitution, the observed Co L_3-edge high/low energy peak ratio systematically decreases, evidencing the incorporation of Fe ions in the octahedral sites. Besides this, after the main Co^{3+} peak, the high energy shoulder is observed around 782.5 eV, which may confirm the low spin state of trivalent cobalt ions [45].

The Fe-L_3 XANES spectra presented in Figure 4c are similar to that of the $ZnFe_2O_4$ reference and are characterized by two distinct spectral features at 708.4 eV and 709.9 eV corresponding to t_2g and e_g sub-bands, respectively [46,47]. From these results, it is clear that Fe^{3+} species were successfully substituted in place of Co^{III}, and remained in the high spin $3d^5$ configuration.
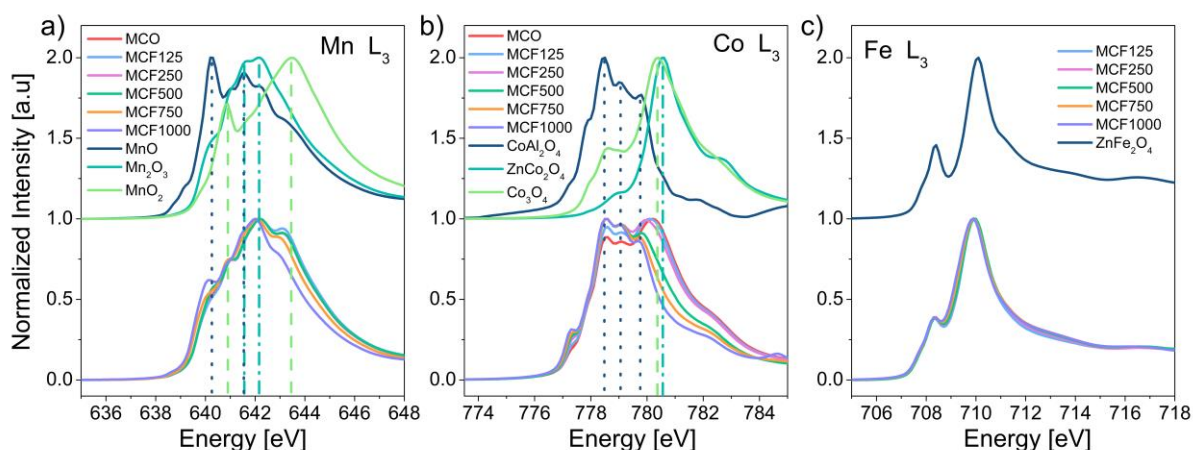
Figure 4. (a) Mn-L$_3$, (b) Co-L$_3$, and (c) Fe-L$_3$ XANES spectra of MnCo$_{2-x}$Fe$_x$O$_s$ powders and several reference materials.

According to group theory, four typical IR bands should be present for cubic II-III spinels. Two of them (ν_1 and ν_2, usually present in the MIR range) can be attributed to vibrations of octahedral units, and two others (ν_3 and ν_4, usually present in the FIR range) can be assigned to mixed octahedral and tetrahedral units within the spinels structure [48,49].

Figure 5 illustrates the spectra within both the MIR (a) and FIR (b) spectral ranges. Multiple bands are present for all spectra below 700 cm^{-1}, including the ν_1 band (Figure 5a) at the highest wavenumbers (630–582 cm^{-1}) and the ν_2 band which is noticeable for samples with either no (MCO) or the lowest Fe doping share (MCF125 and MCF250) in the ca. 540–530 cm^{-1} region. The higher the Fe content, the broader and less visible the ν_2 band becomes. A similar observation of the ν_2 band can be stated for the ν_3 band (Figure 5b), which occurs at around the 360–350 cm^{-1} range. In the end, ν_4 can be found within the 180–171 cm^{-1} range [48].

The most important findings concern the shift of the ν_1 band which is responsible for structural vibrations of the condensed Co^{3+}O$_6$ octahedrons [48]. With the increasing share of introduced Fe, not only does this band shift towards lower wavenumbers, but the value of such a wavenumber shift also corresponds to the expected chemical composition. Taking the boundary examples (MCO and MCF1000) as a sort of scale, 48 cm^{-1} is the maximum shift. Then, during the first doping (MCF125), 1/8 of the maximum doping was executed, which resulted in a shift of 6 cm^{-1}, being exactly 1/8 of 48 cm^{-1}. For the next

specimens, this quantitative approach can also be applied with good accuracy (3/8 for MCF250, 5/8 for MCF500 and 7/8 for MCF750).

When it comes to qualitative interpretation, two factors have to be taken into consideration. Firstly, the broadening of bands occurred, which is due to the partial doping, hence the presence of two cations on the octahedral sites [48,49]. Secondly, based on [48], the direction of the band shift is connected with the M^{III}–O bonding force. The lower the wavenumber, the lower the bond energy. However, in this case, the simple bond energy cannot be applied as different valences and spin states should be taken into account. In [21,50], the authors used the term "covalency" estimated with the N-V parameter (N – number of the unpaired electrons for the metal cation; V – nominal valence state of the metal cation). The lower the N-V parameter (which describes the net ability of the octahedral cation to donate electrons to oxygen), the higher the covalency (in terms of dragging the electron density from oxygen towards the metal cation, thereby forming the stronger, more "covalent" bond). In the case of this work, we observe a decrease in the wavenumbers, which suggests a lower M^{III}–O bonding force expressed by the lower covalency, after the substitution of Co^{3+} cations by Fe^{3+} ones. It stays then in a good agreement with the scenario, in which the electron configuration of degenerated orbitals for Co changes towards the optimal one – assuming that the e_g electron orbital for cobalt cations after the introduction of Fe is free, the N-V parameter for Co is low (0-3=-3 → high covalency), and for Fe is much higher (5-3=2 → low covalency).

In the case of the ν_2 band, also dependent on the trivalent cation nature [48], the shift towards lower wavenumbers can be seen, similar to the ν_1 band. However, all spectra have a very complicated shape in this range, therefore in the next paragraph, more details will be provided taking into account the deconvolution process. When it comes to the ν_3 and ν_4 bands, the former, responsible for complex vibrations of M^{II} and M^{III} [48], can be found along with numerous neighboring bands forming the very complicated contour of the spectrum within the 360–300 cm^{-1} range. Due to the fact that this band is the least informative about the spinels structure, spectra in the aforementioned range were not decomposed. The last evoked band (ν_4), dependent on the mass of tetrahedral cations, could be observed as well. In comparison to the previously described shift for the ν_1 band, this band changes its position in a nearly

negligible way, which suggests that cobalt is being substituted by iron predominantly within the octahedral sites.
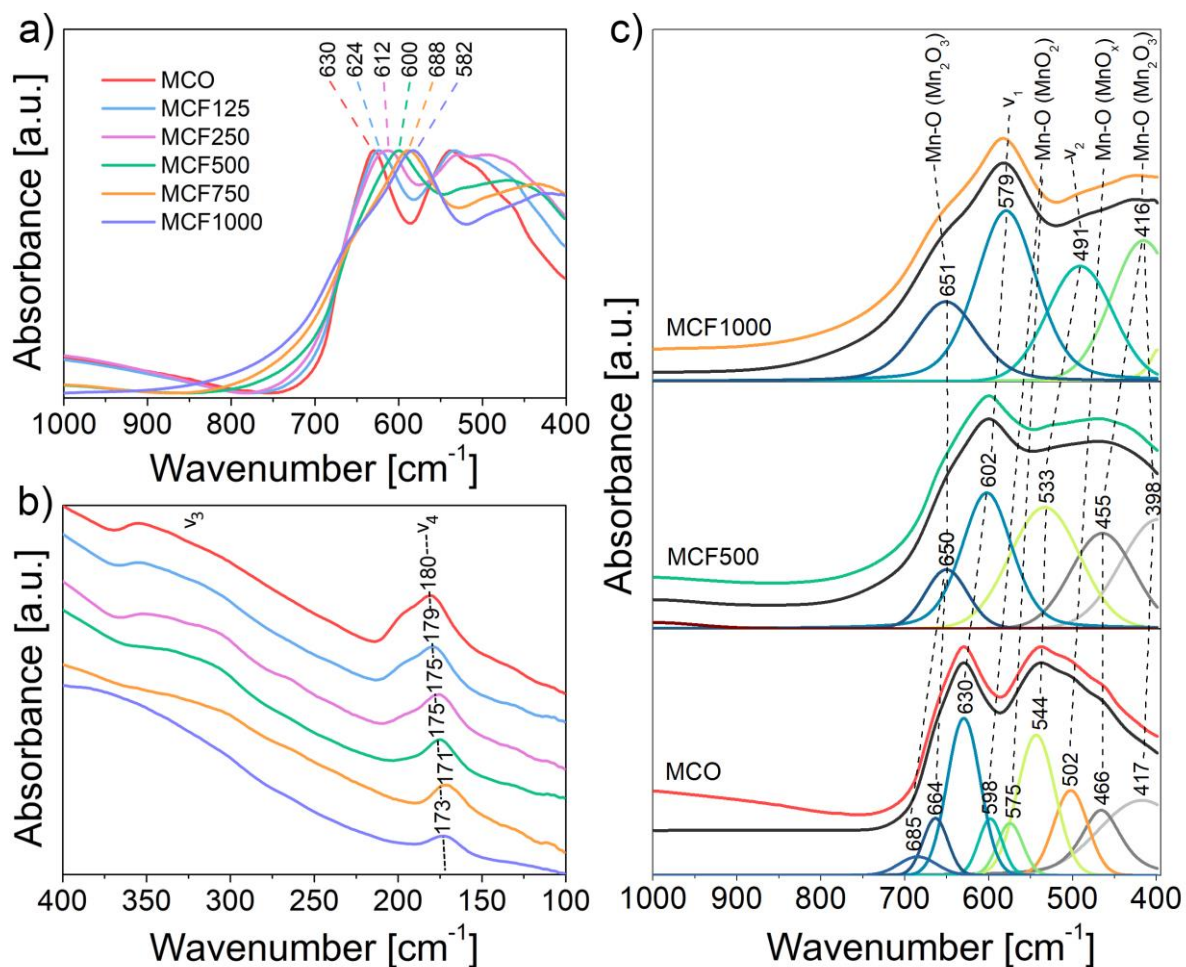
Figure 5. a) Middle Infrared Spectra with marked positions of spinel ν_1 band, b) Far Infrared Spectra with marked positions of spinel ν_4 band, and c) Middle Infrared Spectra after deconvolution process.

To provide more structural details, the MIR spectra for the MCO, MCF500 and MCF1000 samples were deconvoluted below 700 cm^{-1}. Figure 5c demonstrates that apart from the previously described spinel bands, abundant modes are also contributing to the complicated contour of the spectra. Firstly, it is important to recognize that the positions for the ν_1 band are nearly the same as in the case of Figure 5a ($\pm$ 3 cm^{-1}). Secondly, for the stoichiometric Mn-Co spinel, an additional four bands (598, 575, 502 and 466 cm^{-1}) assigned to MnO_2 and MnO_x oxides occurred and disappeared for the Fe-substituted specimens [51,52]. However, as such phases were not detected by the XRD method, and taking into account the much higher sensitivity and detection threshold of MIR compared to XRD, the share of Mn

oxides can be treated as very small, which may actually come from some secondary phases after the synthesis. In contrast, two bands at ca. 660 and 410 cm^{-1} assigned to Mn_2O_3 [51] considerably increased in their intensities, especially for the sample with the highest share of iron, which is in good agreement with the XRD findings. The presence of Mn oxides was also revealed in the FIR range, where numerous bands attributed to the MnO_2 and MnO_x phases can usually be observed [51,52]. In this work, the clearly noticeable band at ca. 200 cm^{-1} decreased in intensity, which confirms the results described for the MIR deconvoluted spectra.

3.2. Electrocatalytic activity. The OER performance of the ball-milled catalyst powders was examined in an alkaline medium (0.1 M KOH). The electrochemical double-layer capacitance (C_{dl}) was analyzed using cyclic voltammetry to determine the electrochemically active surface area (Figure 6a). A slight decrease of C_{dl} with Fe substitution up to x=0.5 in the $MnCo_{2-x}Fe_xO_4$ spinels is noticeable (446 µF and 394 µF for the MCO and MCF500, respectively), whereas further iron incorporation resulted in a threefold C_{dl} decrease for the MCF1000 (146 µF). The obtained data is not consistent with the measured specific surface area. All iron-containing powders exhibited similar surface areas in the range from 22.7 to 23.9 m^2 g^{-1} indicating similar particle size distributions (further supported by the SEM observations). This remark suggests that the number of active sites available for water oxidation decreases with the higher Fe content in the MCF spinel structure, from which it results that iron in the octahedral sites does not catalyze the oxygen evolution reaction as efficiently as cobalt.

To gain insight into the electrode reaction kinetics, electrochemical impedance spectroscopy (EIS) was performed during the OER at a fixed potential. The EIS spectra shown in Figure 6b was fitted using Randles equivalent circuit (presented in Figure S7) to calculate the charge transfer resistance (R_{ct}) between the catalyst and liquid junction during the electrochemical reaction. The lowest R_{ct} of 12.1 Ω was measured for the MCF500, whereas the high Fe content resulted in an increase of R_{ct} to 20.5 Ω and 39.0 Ω for the MCF750 and MCF1000, respectively. It is apparent that the partial Co substitution by Fe cations in the $MnCo_2O_4$ enhances the charge transfer kinetics (R_{ct}) by ~30%. This observation provides the basis for considering the optimally Fe-substituted $MnCo_2O_4$ as superior OER catalysts, despite the slight decrease in the number of active sites indicated by the ECSA studies (Table S4).
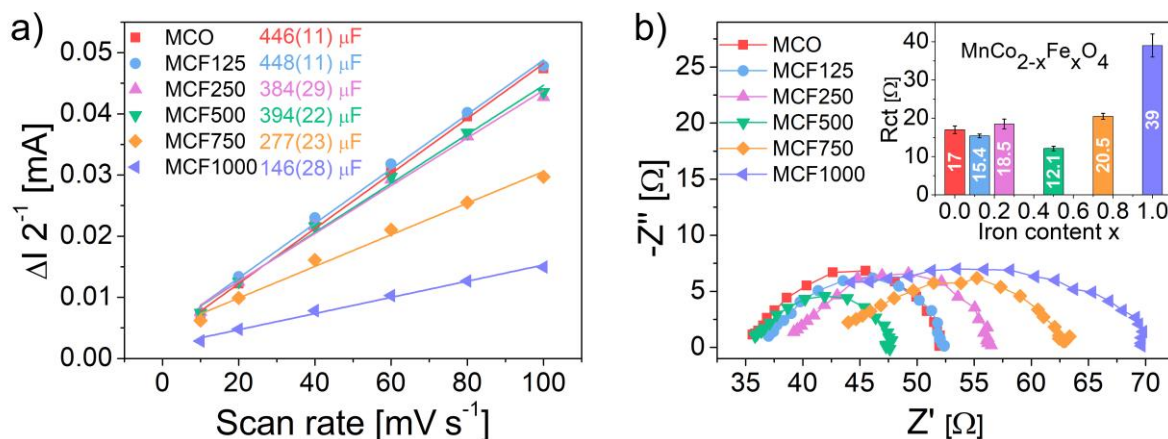
Figure 6. (a) Double-layer capacitance and (b) EIS Nyquist plots recorded at 1.7 V vs RHE. Inset demonstrates calculated charge transfer resistance. Electrochemical tests were performed in 0.1 M KOH electrolyte.

The oxygen evolution reaction geometric current densities of all $MnCo_{2-x}Fe_xO_4$ spinels are shown in Figure 7a. The Glassy Carbon (GC) Rotating Disk Electrode was measured separately to exclude its possible contribution to oxygen electrocatalysis – as expected, negligible activity was observed. The OER electrocatalyst activity is typically characterized by the overpotential (η) needed to deliver the current density of 10 mA cm^{-2} (dashed horizontal line) [53]. The MCO demonstrates an overpotential of 406 mV, which can be reduced to 376 mV for the MCF500 by partial Fe/Co substitution in the spinel structure. Further Fe incorporation results in a sharp overpotential increase up to 447 mV for the MCF1000, implying that Fe cations are not active sites themselves, although an optimal amount can modulate the intrinsic activity of the $MnCo_2O_4$ spinel. The relationship between the octahedral occupation of Fe and OER activity can be seen in the extracted Tafel plots in Figure 7b. The estimated Tafel slope of 44 mV dec^{-1} for the MCF500 is clearly smaller than the 58 mV dec^{-1} for the MCO, implying faster reaction kinetics. The Tafel slopes of the MCF750 and MCF1000 seem to be reduced if compared with the MCO and, from this standpoint, could be considered as more catalytically active, which does not agree with the calculated overpotentials. The explanation for that is the change of the Tafel slope of those two materials at higher overpotentials, i.e. 110 mV dec^{-1} and 180 mV dec^{-1} for the MCF750 and MCF1000, respectively. This observation indicates a possible change in the OER rate-determining step when Fe occupies more than 25% of the available octahedral sites. The lowest

Tafel slope of the MCF500 suggests that the rate-determining step is at the ending part of the multiple-electron transfer oxygen evolution reaction, and it is an indicator of a promising electrocatalyst [54]. Huang et al. reported a similar 45 mV dec^{-1} Tafel slope using an advanced 2D Fe/Co oxide heterostructure. A lower Tafel slope than for single metal 2D structures (67 and 79 mV dec^{-1} for Co(oxides) nanosheets and Fe(oxides) nanochains, respectively) was attributed to the switch of the rate-determining step for OER. The authors propose the switch from $MOH_{ad} + OH^- \rightarrow MO^- + H_2O$ to the electron-proton reaction of $MOH_{ad} + OH^- \rightarrow MO + H_2O + e^-$ rate-determining step [55].
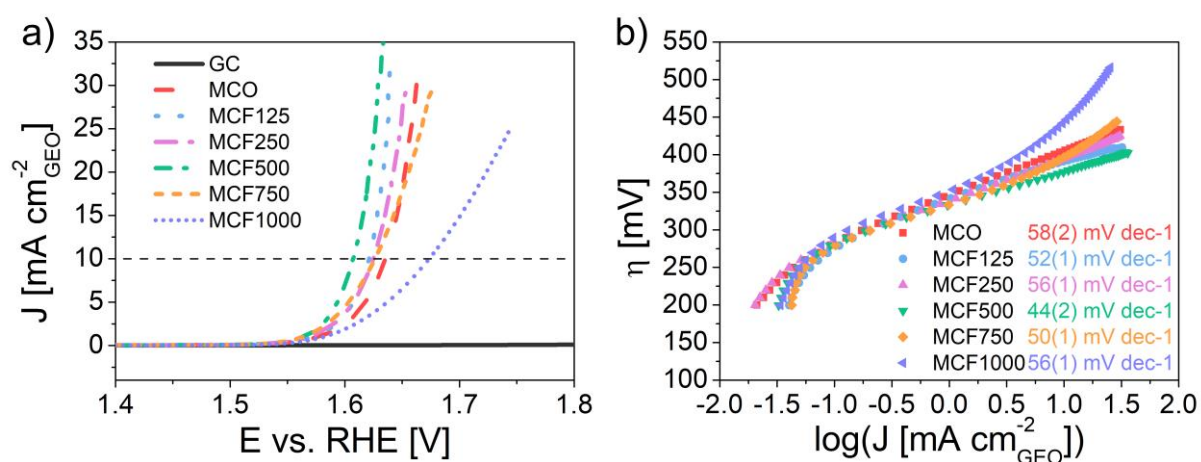
Figure 7. (a) Oxygen evolution polarization curves of $MnCo_{2-x}Fe_xO_4$ catalysts (b) and corresponding Tafel plots measured in O_2-saturated 0.1 M KOH at 10 mV s^{-1} with a rotation speed of 1600 rpm.

Further, the measured polarization curves have been normalized using the BET-specific surface area (Table S2) to exclude the surface area effect and to gain insight into the specific activity of the prepared catalysts. Due to the comparable specific area, the overall trend of increasing activity with moderate Fe substitution in $MnCo_{2-x}Fe_xO_4$ is unchanged, as is shown in Figure 8a.

The reference $MnCo_2O_4$ cation distribution was based on Bordeneuve's report and established as $Co^{2+}_{0.965}Mn^{2+}_{0.035}[Mn^{3+}_{0.78}Mn^{4+}_{0.21}Co^{2+}_{0.21}Co^{III}_{0.8}]$, where Co^{III} means that trivalent cobalt ions are of low spin (LS, $t_{2g}^6 e_g^0$) [44]. As is presented in Figure 1a, iron (as Fe^{3+}) is considered to replace Co^{III} in octahedral sites [56]. This hypothesis was further confirmed by the XANES studies described in the previous part of the article and coincides well with Kim et al., who indicated, by first principle

calculations, that in the MnCoFeO$_4$ spinel Co preferentially occupies tetrahedral while Mn and Fe octahedral sites [24].

To understand the possible origin of the enhanced activity, the activity descriptor based on the e$_g$ occupancy at the octahedral sites in the spinel structure was adopted. The e$_g$ filling of the 3d electron of the surface transition metal cations influencing the binding of OER intermediates to the perovskite oxide surface was proposed by Suntivich et al. and has proven to be a reliable perovskite OER activity descriptor [57–59]. The e$_g$ orbital has a stronger spatial overlap with the oxygen-related adsorbate than the t$_{2g}$ orbital; consequently, the electron transfer between the surface cation and adsorbed intermediate may be more directly promoted by the e$_g$ orbital. Likewise, the e$_g$ occupancy of the active site was proposed to be the activity descriptor for spinels [19,38,60]. Figure 8b presents the e$_g$/t$_{2g}$ electron assignment for Co and Fe octahedrally coordinated cations. The incorporation of octahedrally coordinated Fe cations (t$_{2g}^3$e$_g^2$) increases the overall number of e$_g$ occupancy in the MnCo$_{2-x}$Fe$_x$O$_4$ spinel. As depicted in Figure 8b, the potential required to maintain the current density of 50 µA cm$^{-2}_{ox}$ decreases with the e$_g$ occupancy increase up to 1.1 for the MCF500. The observed volcano plot with the inflection point around unity points to the proposed four-electron/proton-coupled oxygen evolution mechanism presented in Figure 8d. If the e$_g$ occupancy is less than unity, the deprotonation of the oxyhydroxide group during step 3 (M^{m+}-OOH$^-$ + OH$^-$ → M$^{(m+1)+}$-O$_2^{2-}$ + H$_2$O + e$^-$) might be limited. On the contrary, too many electrons in e$_g$ orbitals limits the formation of the O-O bond in the OOH adsorbate during step 2 (M$^{(m+1)+}$-O^{2-} + OH$^-$ → M^{m+}-OOH$^-$ + e$^-$).

For comparison of our results with other literature reports, the OER performance data for recently studied spinel-based electrocatalysts is summarized in Table S5. After Fe incorporation into the MnCo$_2$O$_4$, the OER overpotential is reduced from 510 mV, as obtained by Menezes et al. for MnCo$_2$O$_4$ microspheres or from 406 mV for the MnCo$_2$O$_4$ powder examined in this study to 376 mV for MnCo$_{1.5}$Fe$_{0.5}$O$_4$ [61]. Moreover, MnCo$_{1.5}$Fe$_{0.5}$O$_4$ exhibits a distinctively low Tafel slope of 44 mV dec^{-1} if compared to 75 mV dec^{-1} for Te-Co$_3$O$_4$ or 58 mV dec^{-1} for MnCo$_2$O$_4$ [62].

A similar substitution with the Fe effect was observed by Zhou et al. in a series of ZnFe$_x$Co$_{2-x}$O$_4$ oxides [21]. Up to x = 0.4, the OER-specific activity increase was observed, followed by a systematic decrease

to x = 2.0, creating a volcano-type dependency with respect to the amount of Fe substitution. The authors concluded that the origin of the observed phenomenon is related to the optimal active cation to oxygen covalency, in this case Co-O covalency, as predicted by the *N-V* parameter. Wei et al. investigated $MnCo_2O_4$ cubic spinels synthesized by a solid-state chemistry method at different temperatures (150–900 °C) [19]. Varying heat treatment-induced changes in the Mn valence state. Knowing the valences and cation distribution quantified by EXAFS, the authors were able to estimate the e_g/t_{2g} assignment of the more active cation in the octahedrally coordinated sites, which correlated well with the spinels' OER activity, confirming the applicability of the e_g occupancy descriptor. Likewise, this descriptor is suitable to elucidate the enhanced activity of $MnCo_{2-x}Fe_xO_4$ with moderate Fe substitution.
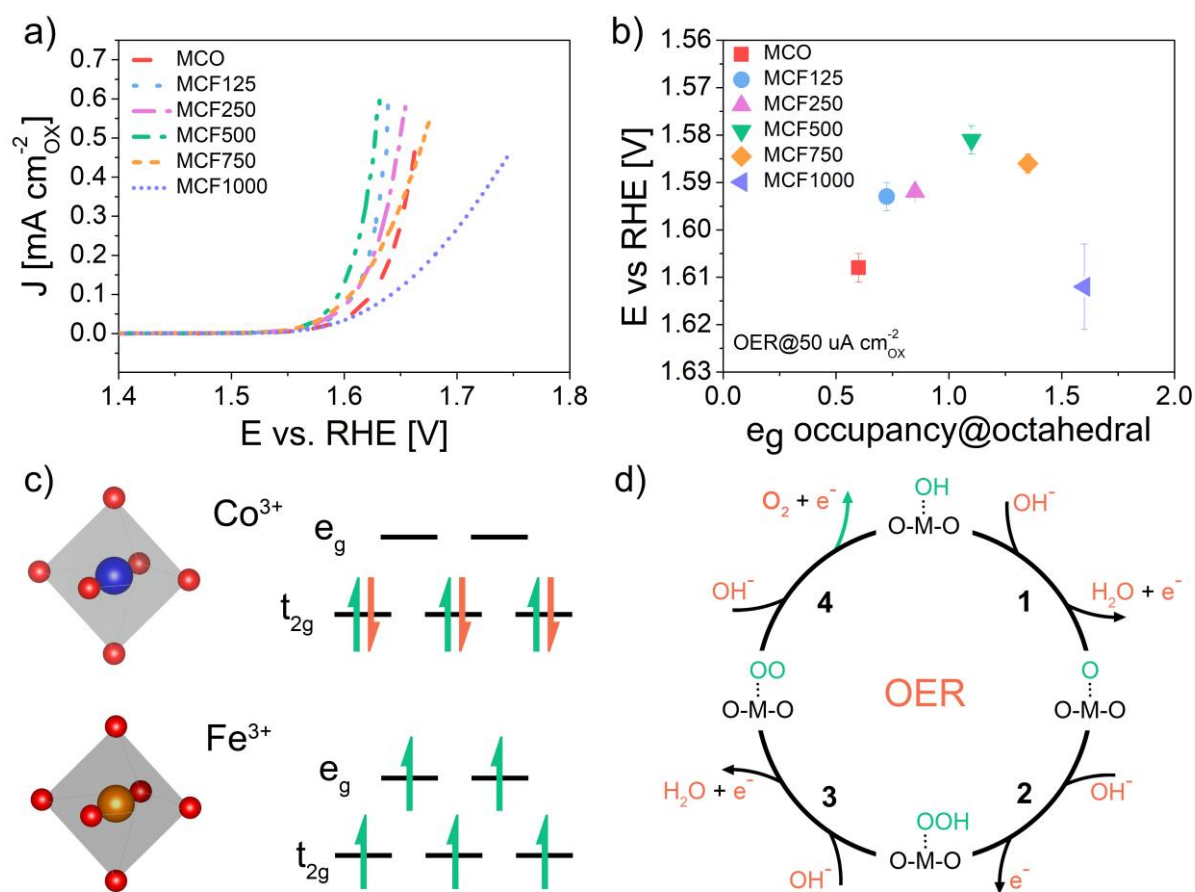
Figure 8. (a) Oxygen evolution polarization curves with current normalized by BET surface area, (b) correlation between OER potentials at 50 μA cm^{-2}_{OX} and e_g occupancy at the octahedral site in $MnCo_{2-x}Fe_xO_4$, (c) e_g/t_{2g} electron assignment for Co and Fe octahedrally coordinated cations, and (d) proposed four-electron/proton-coupled oxygen evolution mechanism.

The long-term electrolyzer stability test of $MnCo_{1.5}Fe_{0.5}O_4$ was performed at a current density of 10 mA cm^{-2} for 48 h (Figure 9). During the test, the catalyst-coated electrode exhibited great stability up to 30 h, and then a slight (4%) increase in voltage was observed. We assume that the performance decrease is related to the degradation of supporting carbon paper. As is shown the test of pure Sigracet carbon paper ended rapidly after 1 h with degradation of the electrode (Figure S8). Similar but slower and less pronounced degradation of catalyst-coated electrode was observed for $MnCo_{1.5}Fe_{0.5}O_4$ (Figure S9).
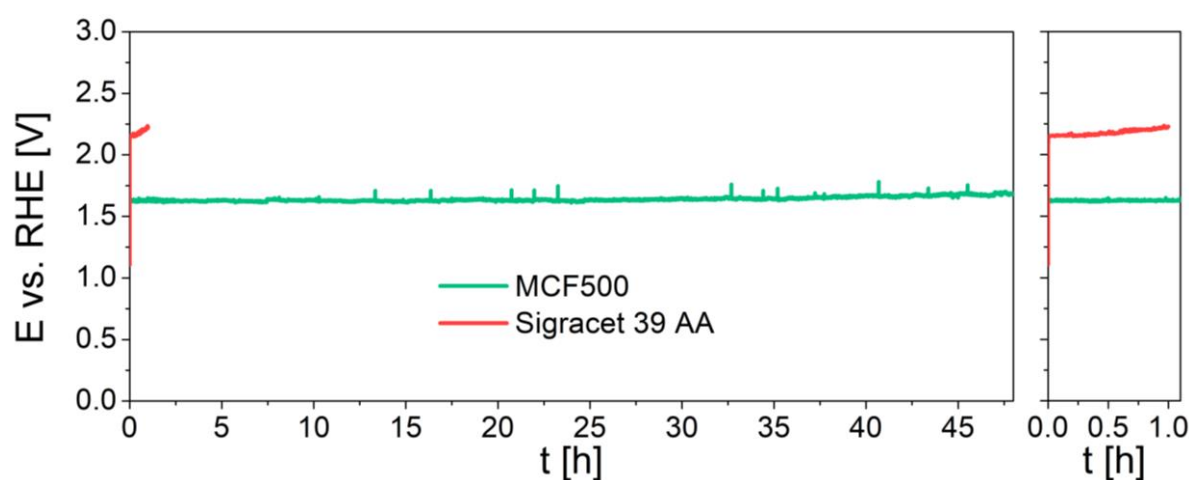
Figure 9. Chronopotentiometric durability test at 10 mA cm^{-2}

4. CONCLUSIONS

The present research examined the effect of Fe ions at octahedral sites in $MnCo_2O_4$ spinel on the physicochemical properties and electrochemical activity. Spectroscopic studies (XAS and FTIR) confirmed the successful substitution of Co ions by Fe ions in octahedrally coordinated positions in $MnCo_{2-x}Fe_xO_4$ spinel powders synthesized using an EDTA-CA sol-gel method.

This study found that moderate Fe incorporation in $MnCo_2O_4$ spinel enhances the catalytic activity towards OER by lowering the charge transfer resistance and moderating the influence of the rate-determining steps during the oxidation cycle. We found that an optimal amount of incorporated Fe into the octahedral sites improves the OER performance by the 30 mV decrease of overpotential needed to achieve a 10 mA cm$^{-2}_{GEO}$ current density compared to the benchmark $MnCo_2O_4$. Tafel slope analysis indicates the possible change of the OER rate-determining step when Fe occupies more than 25% of the

available octahedral sites. The OER-specific activity exhibits a volcano-type shape as a function of the e_g occupancy at octahedral sites. Overall, this work supports the idea that e_g occupancy at octahedral sites can be used as the activity descriptor for spinels. The strategy of tuning the optimal e_g configurations by transition metal substitution in the spinel's octahedral sites is a promising tool for the design of superior OER catalysts.

AUTHOR INFORMATION

Corresponding Author

*E-mail: krystian.lankauf@pg.edu.pl

Notes

The authors declare no competing financial interest.

ACKNOWLEDGMENTS

REFERENCES

[1]   Farrukh S, Fan X, Mustafa K, Hussain A, Ayoub M, Younas M. Nanotechnology and the Generation of Sustainable Hydrogen. 2021.

[2]   Platzer MF, Sarigul-Klijn N. Conversion of Hydrogen to Electricity. Green Energy Sh. Concept Renew. Energy from Wind Over Water, Cham: Springer International Publishing; 2021, p. 99–101. https://doi.org/10.1007/978-3-030-58244-9_24.

[3]   Klingmann J, Andersson M. Hydrogen and Hydrogen-Rich Fuels: Production and Conversion to Electricity. In: Gupta AK, De A, Aggarwal SK, Kushari A, Runchal A, editors. Innov. Sustain. Energy Clean. Environ., Singapore: Springer Singapore; 2020, p. 219–33. https://doi.org/10.1007/978-981-13-9012-8_10.

[4]   Fabbri E, Habereder A, Waltar K, Kötz R, Schmidt TJ. Developments and perspectives of oxide-based catalysts for the oxygen evolution reaction. Catal Sci Technol 2014;4:3800–21. https://doi.org/10.1039/c4cy00669k.

[5]   Liu L, Xiao Y. Theoretical exploration electrocatalytic active of spinel M2CoO4 (M = Co, Fe

and Ni) as efficient catalyst for water splitting. Comput Mater Sci 2021;187:110082. https://doi.org/10.1016/j.commatsci.2020.110082.

[6] Du J, Qian Y, Wang L, Yang H, Kang DJ. Facile synthesis of copper sulfides on copper foam as an efficient electrocatalyst for oxygen evolution reaction. Mater Today Commun 2020;25:101585. https://doi.org/10.1016/j.mtcomm.2020.101585.

[7] Li M, Wang L, Qian Y, Du J. Facile synthesis of MoS2/CuS nanoflakes as high performance electrocatalysts for hydrogen evolution reaction. Int J Hydrogen Energy 2022;47:5319–25. https://doi.org/10.1016/j.ijhydene.2021.11.182.

[8] Chen C, Tuo Y, Lu Q, Lu H, Zhang S, Zhou Y, et al. Hierarchical trimetallic Co-Ni-Fe oxides derived from core-shell structured metal-organic frameworks for highly efficient oxygen evolution reaction. Appl Catal B Environ 2021;287:119953. https://doi.org/10.1016/j.apcatb.2021.119953.

[9] Gonçalves JM, Silva MNT, Naik KK, Martins PR, Rocha DP, Nossol E, et al. Multifunctional spinel MnCo2O4based materials for energy storage and conversion: a review on emerging trends, recent developments and future perspectives. J Mater Chem A 2021;9:3095–124. https://doi.org/10.1039/d0ta11129e.

[10] O'Neill HSC, Navrotsky A. Simple spinels: crystallographic parameters, cation radii, lattice energies, and cation distribution. Am Mineral 1983;68:181–94.

[11] Saito T. Chemistry of Transition Metals. Introd Chem Ser 1996:110–53.

[12] Yunasfi, Mulyawan A, Mashadi, Suyanti, Ari Adi W. Synthesis of NiCe Fe(2-)O4 ($0 \leq x \leq 0.05$) as Microwave Absorbing Materials via Solid-State Reaction Method. J Magn Magn Mater 2021;532:167985. https://doi.org/10.1016/j.jmmm.2021.167985.

[13] Xuan S, Wang X, Tian Y, Hao J. Properties of magnesium-aluminate spinel derived from bauxite and magnesia. Int J Appl Ceram Technol 2021:1–8. https://doi.org/10.1111/ijac.13740.

[14] Li C, Han X, Cheng F, Hu Y, Chen C, Chen J. Phase and composition controllable synthesis of cobalt manganese spinel nanoparticles towards efficient oxygen electrocatalysis. Nat Commun 2015;6:1–8. https://doi.org/10.1038/ncomms8345.

[15] Paul B, Bhanja P, Sharma S, Yamauchi Y, Alothman ZA, Wang ZL, et al. Morphologically controlled cobalt oxide nanoparticles for efficient oxygen evolution reaction. J Colloid Interface Sci 2021;582:322–32. https://doi.org/10.1016/j.jcis.2020.08.029.

[16] Waqas M, El Kasmi A, Wang Y, Mountapmbeme Kouotou P, Tian ZY. CVD synthesis of Cu-doped cobalt spinel thin film catalysts for kinetic study of propene oxidation. Colloids Surfaces A Physicochem Eng Asp 2018;556:195–200. https://doi.org/10.1016/j.colsurfa.2018.08.006.

[17] El Kasmi A, Waqas M, Mountapmbeme Koutou P, Tian Z. Cu-Promoted Cobalt Oxide Film Catalyst for Efficient Gas Emissions Abatement. J Therm Sci 2018;28:225–31. https://doi.org/10.1007/s11630-019-1093-9.

[18] Sheil R, Butts D, Jungjohann K, Yoo J, Dunn B, Chang JP. Plasma enhanced atomic layer deposition of thin film Li 1+x Mn 2−x O 4 for realization of all solid-state 3D lithium-ion microbatteries . J Vac Sci Technol A 2021;39:012408. https://doi.org/10.1116/6.0000644.

[19] Wei C, Feng Z, Scherer GG, Barber J, Shao-Horn Y, Xu ZJ. Cations in Octahedral Sites: A Descriptor for Oxygen Electrocatalysis on Transition-Metal Spinels. Adv Mater 2017;29:1–8. https://doi.org/10.1002/adma.201606800.

[20] Wang W, Kuai L, Cao W, Huttula M, Ollikkala S, Ahopelto T, et al. Mass-Production of Mesoporous MnCo2O4 Spinels with Manganese(IV)- and Cobalt(II)-Rich Surfaces for Superior Bifunctional Oxygen Electrocatalysis. Angew Chemie - Int Ed 2017;56:14977–81.

https://doi.org/10.1002/anie.201708765.

[21] Zhou Y, Sun S, Song J, Xi S, Chen B, Du Y, et al. Enlarged Co☐O Covalency in Octahedral Sites Leading to Highly Efficient Spinel Oxides for Oxygen Evolution Reaction. Adv Mater 2018;30:1–7. https://doi.org/10.1002/adma.201802912.

[22] Liu Y, Fergus JW, Wang K, Dela Cruz C. Crystal Structure, Chemical Stabilities and Electrical Conductivity of Fe-Doped Manganese Cobalt Spinel Oxides for SOFC Interconnect Coatings. J Electrochem Soc 2013;160:F1316–21. https://doi.org/10.1149/2.114311jes.

[23] Elkholy AE, El-Taib Heakal F, Allam NK. Nanostructured spinel manganese cobalt ferrite for high-performance supercapacitors. RSC Adv 2017;7:51888–95. https://doi.org/10.1039/c7ra11020k.

[24] Kim H, Seo DH, Kim H, Park I, Hong J, Park KY, et al. Multicomponent effects on the crystal structures and electrochemical properties of spinel-structured M 3O 4 (M = Fe, Mn, Co) anodes in lithium rechargeable batteries. Chem Mater 2012;24:720–5. https://doi.org/10.1021/cm2036794.

[25] Lankauf K, Cysewska K, Karczewski J, Mielewczyk-Gryń A, Górnicka K, Cempura G, et al. MnxCo3-xO4 spinel oxides as efficient oxygen evolution reaction catalysts in alkaline media. Int J Hydrogen Energy 2020;5. https://doi.org/10.1016/j.ijhydene.2020.03.188.

[26] Rodriguez-Carvajal J. Recent advances in magnetic structure determination by neutron powder diffraction. Phys B 1993:55–69. https://doi.org/doi.org/10.1016/0921-4526(93)90108-I.

[27] Toby BH, Von Dreele RB. GSAS-II: The genesis of a modern open-source all purpose crystallography software package. J Appl Crystallogr 2013;46:544–9. https://doi.org/10.1107/S0021889813003531.

[28] Meena PL, Kumar R, Sreenivas K. Rietveld Refinement and Spectroscopic Analysis of Co3-xMnxO4 (0.1≤ x≤ 1.0) Ceramic Compositions. Int J Phys Chem Math Sci 2014;3:7.

[29] König U, Chol G. Röntgenbeugungs- und Neutronenbeugungsuntersuchungen an Ferriten der reihe MnxZn1−xFe2O4. J Appl Crystallogr 1968;1:124–6. https://doi.org/10.1107/s0021889868005145.

[30] Madej E, Pitala K, Kozio A, Sikora M, Spiridis N, Sl T, et al. Nuclear Inst . and Methods in Physics Research , B The first experimental results from the 04BM (PEEM / XAS) beamline at Solaris 2021;492:43–8.

[31] Handke M, Mozgawa W, Nocuń M. Specific features of the IR spectra of silicate glasses. J Mol Struct 1994;325:129–36. https://doi.org/https://doi.org/10.1016/0022-2860(94)80028-6.

[32] Lankauf K, Mroziński A, Błaszczak P, Górnicka K, Ignaczak J, Łapiński M, et al. The effect of Fe on chemical stability and oxygen evolution performance of high surface area SrTix-1FexO3-δ mixed ionic-electronic conductors in alkaline media. Int J Hydrogen Energy 2021;46:28575–90. https://doi.org/https://doi.org/10.1016/j.ijhydene.2021.06.088.

[33] McCrory CCL, Jung S, Peters JC, Jaramillo TF. Benchmarking heterogeneous electrocatalysts for the oxygen evolution reaction. J Am Chem Soc 2013;135:16977–87. https://doi.org/10.1021/ja407115p.

[34] Wei C, Rao RR, Peng J, Huang B, Stephens IEL, Risch M, et al. Recommended Practices and Benchmark Activity for Hydrogen and Oxygen Electrocatalysis in Water Splitting and Fuel Cells. Adv Mater 2019;1806296:1–24. https://doi.org/10.1002/adma.201806296.

[35] Niu S, Li S, Du Y, Han X, Xu P. How to Reliably Report the Overpotential of an Electrocatalyst. ACS Energy Lett 2020;5:1083–7. https://doi.org/10.1021/acsenergylett.0c00321.

[36] Purwanto A, Fajar A, Mugirahardjo H, Fergus JW, Wang K. Cation distribution in spinel

(Mn,Co,Cr)3O4 at room temperature. J Appl Crystallogr 2010;43:394–400. https://doi.org/10.1107/S0021889810008150.

[37] Biesinger MC, Payne BP, Grosvenor AP, Lau LWM, Gerson AR, Smart RSC. Resolving surface chemical states in XPS analysis of first row transition metals, oxides and hydroxides: Cr, Mn, Fe, Co and Ni. Appl Surf Sci 2011;257:2717–30. https://doi.org/10.1016/j.apsusc.2010.10.051.

[38] Gao X, Liu J, Sun Y, Wang X, Geng Z, Shi F, et al. Optimized Co2+(Td)-O-Fe3+(Oh) electronic states in a spinel electrocatalyst for highly efficient oxygen evolution reaction performance. Inorg Chem Front 2019;6:3295–301. https://doi.org/10.1039/c9qi00852g.

[39] Mountapmbeme Kouotou P, Vieker H, Tian ZY, Tchoua Ngamou PH, El Kasmi A, Beyer A, et al. Structure-activity relation of spinel-type Co-Fe oxides for low-temperature CO oxidation. Catal Sci Technol 2014;4:3359–67. https://doi.org/10.1039/c4cy00463a.

[40] Nikolic M V., Vasiljevic ZZ, Lukovic MD, Pavlovic VP, Krstic JB, Vujancevic J, et al. Investigation of ZnFe 2 O 4 spinel ferrite nanocrystalline screen-printed thick films for application in humidity sensing. Int J Appl Ceram Technol 2019;16:981–93. https://doi.org/10.1111/ijac.13190.

[41] Yu F, Yang J, Ma J, Du J, Zhou Y. Preparation of nanosized CoAl2O4 powders by sol-gel and sol-gel-hydrothermal methods. J Alloys Compd 2009;468:443–6. https://doi.org/10.1016/j.jallcom.2008.01.018.

[42] Kim TW, Woo MA, Regis M, Choi KS. Electrochemical synthesis of spinel type ZnCo2O4 electrodes for use as oxygen evolution reaction catalysts. J Phys Chem Lett 2014;5:2370–4. https://doi.org/10.1021/jz501077u.

[43] Wang HY, Hung SF, Chen HY, Chan TS, Chen HM, Liu B. In Operando Identification of Geometrical-Site-Dependent Water Oxidation Activity of Spinel Co3O4. J Am Chem Soc 2016;138:36–9. https://doi.org/10.1021/jacs.5b10525.

[44] Bordeneuve H, Tenailleau C, Guillemet-Fritsch S, Smith R, Suard E, Rousset A. Structural variations and cation distributions in Mn3-xCoxO4 (0 ≤ x ≤ 3) dense ceramics using neutron diffraction data. Solid State Sci 2010;12:379–86. https://doi.org/10.1016/j.solidstatesciences.2009.11.018.

[45] Istomin SY, Tyablikov OA, Kazakov SM, Antipov E V., Kurbakov AI, Tsirlin AA, et al. An unusual high-spin ground state of Co3+ in octahedral coordination in brownmillerite-type cobalt oxide. Dalt Trans 2015;44:10708–13. https://doi.org/10.1039/c4dt03670k.

[46] Singh JP, Kaur B, Sharma A, Kim SH, Gautam S, Srivastava RC, et al. Mechanistic insights into the interaction between energetic oxygen ions and nanosized ZnFe2O4: XAS-XMCD investigations. Phys Chem Chem Phys 2018;20:12084–96. https://doi.org/10.1039/c8cp00368h.

[47] Kumar S, Kim YJ, Koo BH, Sharma SK, Vargas JM, Knobel M, et al. Structural and magnetic properties of chemically synthesized Fe doped ZnO. J Appl Phys 2009;105:1–4. https://doi.org/10.1063/1.3073933.

[48] Preudhomme J, Tarte P. Infrared studies of spinels—III: The normal II–III spinels. Spectrochim Acta Part A Mol Spectrosc 1971;27:1817–35. https://doi.org/https://doi.org/10.1016/0584-8539(71)80235-0.

[49] Basak D, Ghose J. Infrared studies on some substituted copper chromite spinels. Spectrochim Acta Part A Mol Spectrosc 1994;50:713–8. https://doi.org/https://doi.org/10.1016/0584-8539(94)80008-1.

[50] Rong X, Parolin J, Kolpak AM. A Fundamental Relationship between Reaction Mechanism and Stability in Metal Oxide Catalysts for Oxygen Evolution. ACS Catal 2016;6:1153–8. https://doi.org/10.1021/acscatal.5b02432.

[51]   Julien CM, Massot M, Poinsignon C. Lattice vibrations of manganese oxides: Part I. Periodic structures. Spectrochim Acta - Part A Mol Biomol Spectrosc 2004;60:689–700. https://doi.org/10.1016/S1386-1425(03)00279-8.

[52]   Parikh SJ, Chorover J. FTIR spectroscopic study of biogenic Mn-oxide formation by Pseudomonas putida GB-1. Geomicrobiol J 2005;22:207–18. https://doi.org/10.1080/01490450590947724.

[53]   McCrory CCL, Jung S, Ferrer IM, Chatman SM, Peters JC, Jaramillo TF. Benchmarking Hydrogen Evolving Reaction and Oxygen Evolving Reaction Electrocatalysts for Solar Water Splitting Devices. J Am Chem Soc 2015;137:4347–57. https://doi.org/10.1021/ja510442p.

[54]   Suen NT, Hung SF, Quan Q, Zhang N, Xu YJ, Chen HM. Electrocatalysis for the oxygen evolution reaction: Recent development and future perspectives. Chem Soc Rev 2017;46:337–65. https://doi.org/10.1039/c6cs00328a.

[55]   Huang Y, Yang R, Anandhababu G, Xie J, Lv J, Zhao X, et al. Cobalt/Iron(Oxides) Heterostructures for Efficient Oxygen Evolution and Benzyl Alcohol Oxidation Reactions. ACS Energy Lett 2018;3:1854–60. https://doi.org/10.1021/acsenergylett.8b01071.

[56]   Talic B, Hendriksen PV, Wiik K, Lein HL. Thermal expansion and electrical conductivity of Fe and Cu doped MnCo2O4 spinel. Solid State Ionics 2018;326:90–9. https://doi.org/10.1016/j.ssi.2018.09.018.

[57]   Suntivich J, May KJ, Gasteiger HA, Goodenough JB, Shao-Horn Y. A perovskite oxide optimized for oxygen evolution catalysis from molecular orbital principles. Science (80-) 2011;334:1383–5. https://doi.org/10.1126/science.1212858.

[58]   Han B, Risch M, Lee YL, Ling C, Jia H, Shao-Horn Y. Activity and stability trends of perovskite oxides for oxygen evolution catalysis at neutral pH. Phys Chem Chem Phys 2015;17:22576–80. https://doi.org/10.1039/c5cp04248h.

[59]   Zhou S, Miao X, Zhao X, Ma C, Qiu Y, Hu Z, et al. Engineering electrocatalytic activity in nanosized perovskite cobaltite through surface spin-state transition. Nat Commun 2016;7:1–7. https://doi.org/10.1038/ncomms11510.

[60]   Liu Y, Ying Y, Fei L, Liu Y, Hu Q, Zhang G, et al. Valence engineering via selective atomic substitution on tetrahedral sites in spinel oxide for highly enhanced oxygen evolution catalysis. J Am Chem Soc 2020;141:8136–45. https://doi.org/10.1021/jacs.8b13701.

[61]   Menezes PW, Indra A, Sahraie NR, Bergmann A, Strasser P, Driess M. Cobalt-manganese-based spinels as multifunctional materials that unify catalytic water oxidation and oxygen reduction reactions. ChemSusChem 2015;8:164–7. https://doi.org/10.1002/cssc.201402699.

[62]   Harada M, Kotegawa F, Kuwa M. Structural Changes of Spinel MCo2O4(M = Mn, Fe, Co, Ni, and Zn) Electrocatalysts during the Oxygen Evolution Reaction Investigated by in Situ X-ray Absorption Spectroscopy. ACS Appl Energy Mater 2022;5:278–94. https://doi.org/10.1021/acsaem.1c02824.